Li-Substituted Layered Spinel Cathode Material for Sodium Ion Batteries

Changjian Deng,[†] Paige Skinner,[†] Yuzi Liu,[‡] Meiling Sun,[‖] Wei Tong,[‖] Chunrong Ma,[†,§] Miu Lun Lau,[†] Riley Hunt,[†] Pete Barnes,[†] Jing Xu,*[,⊥] and Hui Xiong*[,†,#]

[†]Micron School of Materials Science and Engineering, Boise State University, 1910 University Dr., Boise, Idaho 83725, United States

[‡]Center for Nanoscale Materials, Argonne National Laboratory, Lemont, Illinois 60439, United States

[§]Shanghai Electrochemical Energy Devices Research Center, School of Chemistry and Chemical Engineering, Shanghai Jiao Tong University, Shanghai 200240, China

[‖]Energy Storage and Distributed Resources Division, Lawrence Berkeley National Laboratory, Berkeley, California 94720, United States

[⊥]Department of Materials Science and Engineering, Iowa State University, Ames, Iowa 50011, United States

[#]Center for Advanced Energy Studies, 995 University Boulevard, Idaho Falls, Idaho 83401, United States

S *Supporting Information*

ABSTRACT: The O3-type layered $Na(Ni_xFe_yMn_z)O_2$ $(0 < x, y, z < 1)$ cathode materials have attracted great interest in sodium ion batteries due to the abundance and cost of raw materials and their high specific capacities. However, the cycling stability and rate capability at high voltages (> 4.0 V) of these materials remain an issue. In this work, we successfully synthesized a Li-substituted layered-tunneled (O3-spinel) intergrowth cathode (LS-NFM) to address these issues. The remarkable structural compatibility and connectivity of the two phases were confirmed by X-ray diffraction (XRD), selected area electron diffraction (SAED), and high-resolution transmission electron microscopy (HRTEM). The LS-NFM electrode reached a discharge capacity of 96 mAh g^{-1} with a capacity retention of 86% after 100 cycles at a current rate of 100 mA g^{-1} in a voltage window of 2.0−4.2 V. Moreover, the LS-NFM cathode exhibited an enhanced rate capability in comparison to the undoped single-phased layered cathode (NFM). The enhanced rate capability of LS-NFM can be explained by the significantly increased effective Na^+ diffusivity measured by the galvanostatic intermittent titration technique (GITT) compared to the undoped control NFM cathode, which can be ascribed to the improved charge transport kinetics through shortened diffusion path by direct connection between the 3D channels in the spinel phase and 2D channels in the layered phase. The results from *ex situ* hard/soft X-ray adsorption spectroscopy (XAS) suggest that the capacity of the LS-NFM cathode is mainly associated with the Ni^{2+}/Ni^{4+} redox couple and slightly from the Fe^{3+}/Fe^{4+} redox couple. The voltage profile of the LS-NFM cathode exhibits a reversible plateau above 4.0 V, indicating great stability at high voltages and structural stabilization by the spinel phase. In addition to the substitution of various transition metals, or the modification of the stoichiometry of each transition metal, this study provides a new strategy to improve electrochemical performance of layered cathode materials for sodium ion batteries.
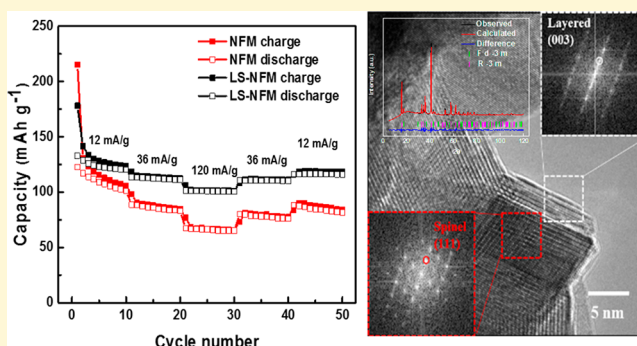
INTRODUCTION

Because of the high abundance and low cost of sodium, the sodium ion battery (SIB) has been considered as an attractive technology for the next-generation, large-scale energy storage systems (EES) in support of reliable, robust, and cost-effective electrical power grids using renewable energy sources such as solar and wind.[1−4] Although the energy/power density of SIBs may not exceed those of the current leading lithium ion battery (LIB) technology due to the heavier atomic weight and larger ionic size of sodium compared with lithium,[2,5−8] the wide and abundant natural reserve of Na raw materials contrasts the limited, and more costly, Li-based minerals.[4,9−14] Owing to

their relatively high capacity from the close-packed structure, layered sodium transition metal oxides Na_xTMO_2 ($x \le 1$, TM = transition metal) have received the most attention for research and development.[1−3,15] Layered Na_xTMO_2 prefer O3-type stacking sequence at high Na contents (e.g., $x \sim 0.9$−1.0).[15] Among O3-type layered oxides, $Na(Ni_xFe_yMn_z)O_2$ cathode is of great interest due to the utilization of cheap, abundant, and environmentally friendly transition metals of Fe

and Mn as well as significant improvement in stability and energy density compared with the NaFeO$_2$ cathode.[16] The ternary Fe-substituted O3−Na(Ni$_{1/3}$Fe$_{1/3}$Mn$_{1/3}$)O$_2$ cathode was first introduced by Kim et al. with a reversible capacity of 100 mA h g^{-1} for 150 cycles (1.5−4.0 V).[10] Since then, systematic studies with various Fe substitutions in ternary O3-type materials were conducted by Yabuuchi et al.[17] and Ding et al.,[18] exhibiting ∼130 mAh g^{-1} reversible capacity for Fe = 0.4 and Fe = 0.2, respectively. Moreover, large-scale synthesis of Na(Ni$_{1/3}$Fe$_{1/3}$Mn$_{1/3}$)O$_2$ has been achieved in a pouch cell, showing capacity retention of 73% after 500 cycles.[19]

Although the technology of O3-type layered cathodes for SIBs has rapidly developed, the cycling stability of such materials especially at high voltages (above 4.0 V vs Na/Na$^+$) remains an issue.[20] The Na$^+$/vacancy ordering in O3 structures triggers the phase transitions by the gliding of TMO$_2$ layers through vector (1/3, 2/3, 0) without breaking TM−O bonds.[21] With partial extraction of Na ions during charging process, the O3 structure gradually transforms to the P3 structure; namely, Na ions are located at prismatic sites with a stacking sequence of AB-BC-CA.[1] It was found that phase transition in O3-type layered cathodes plays a crucial role in their charge storage property and cycling stability. Particularly, the existence or reversibility of the phase transitions directly affects the stability of materials during Na insertion and extraction. Recently, several groups have reported that the overall electrochemical performance of O3-type layered cathodes can be enhanced by lithium substitution.[22−25] When Li ions are introduced to the O3-type layered cathodes, Li ions are thermodynamically favored at the transition metal sites due to the similarity of its ionic radii (0.76 Å) to that of the transition metals (∼0.5−0.7 Å).[23,26] Therefore, the traditional design strategy of Li-substituted layered cathodes follows the rule that the stoichiometric ratio of Na over the sum of transition metals and Li equals 1, so that the as-prepared cathodes maintain single-phased layered structures. Xu et al. investigated NaLi$_x$Ni$_{1/3-x}$Mn$_{1/3+x}$Co$_{1/3-x}$O$_2$ (x = 0.07, 0.13, and 0.2), and the optimal performance was obtained by x = 0.07 with high reversible capacity of 147 mAh g^{-1} and excellent rate capability.[25] The *ex situ* synchrotron X-ray diffraction (XRD) suggested that the O3 phase is maintained upon cycling, leading to good capacity retention and excellent rate performance.[25] Oh et al. reported O3-type Na-[Li$_{0.05}$(Ni$_{0.25}$Fe$_{0.25}$Mn$_{0.5}$)$_{0.95}$]O$_2$ cathode with improved capacity retention and structural stability.[23] The XRD results suggested that the phase transition from hexagonal O3 to monoclinic P′3 was delayed in Li substituted cathode, leading to an enhanced stability.[23]

In addition to the single-phased Li-substituted O3-type layered cathodes, Lee et al. varied the Li content and obtained the layered P2/O3 intergrowth cathode that exhibited a synergistic effect to improve Na$^+$ diffusion for high rate performance.[27] Intergrowth electrode materials have also been studied by other groups. Chen et al. prepared stable layered P3/P2 Na$_{0.66}$Co$_{0.5}$Mn$_{0.5}$O$_2$ cathode materials with outstanding structural flexibility and electrochemical performance.[28] Zheng et al. demonstrated that NaLi$_{0.1}$Ni$_{0.35}$Mn$_{0.55}$O$_2$ exhibited O3/O′3 structure and the presence of the O′3 phase, originating from Li substitution, hindered the O3−P3 phase transformation, thus improving capacity retention, such that 85% of capacity was maintained after 100 cycles.[24] Bianchini et al. prepared layered P2−O3 Na$_{2/3}$Li$_{0.18}$Mn$_{0.8}$Fe$_{0.2}$O$_2$ cathode derived from earth abundant elements, where the electrode

delivered a capacity of 125 and 105 mA h g^{-1} at C/10 and 1C rates, respectively, with a Coulombic efficiency of 95−99.9% over 100 cycles.[29]

Aside from the layered intergrowth cathodes, Gao et al. reported a novel design of the mixed layered-tunneled P2+T phase Na$_x$Co$_{0.1}$Mn$_{0.9}$O$_2$ (0.44 ≤ x ≤ 0.7) with interface-rich characteristic for high performance sodium storage, whereby the tunneled T phase offers fast Na ion diffusivity and excellent structural stability and the layered P2 phase contributes to high specific capacity.[30] In addition, the P2−T interface offers additional channels and active sites for charge storage and transfer. The specific capacity, structural stability, rate capability, and Na ion diffusivity were significantly improved in the P2+T phase cathode compared with single P2 or T phase cathodes.[30]

In addition to T phase, the postspinel NaMn$_2$O$_4$ cathode material with tunneled structure showed high structural stability and Na mobility for sodium ion batteries based on both computational and experimental studies.[31,32] The postspinel NaMn$_2$O$_4$ was prepared under high pressure and it exhibited 94% capacity retention after 200 cycles. The stable cycling performance was attributed to the suppression of the Jahn−Teller distortion due to the high barrier of structural rearrangement of MnO$_6$ octahedrons.

Inspired by the advantages of O3−Na(Ni$_x$Fe$_y$Mn$_z$)O$_2$ cathode materials, the design strategies of Li substitution, layered-tunneled intergrown phases, and tunneled spinel phase with improved structural stability and Na mobility, we report here a Li-substituted layered-tunneled O3/spinel Na-(Ni$_x$Fe$_y$Mn$_z$)O$_2$ cathode material, Na$_{0.87}$Li$_{0.25}$Ni$_{0.4}$Fe$_{0.2}$Mn$_{0.4}$O$_{2+\delta}$ (LS-NFM), for enhanced sodium ion storage and cycling stability. The LS-NFM electrode was prepared by adjusting the stoichiometric ratio of the Na ion over the sum of Li and transition metal ions below 1. The Rietveld refinement of XRD data indicated that the cathode is composed of 94% layered and 6% spinel components. The great structural compatibility and connectivity of the two phases are confirmed by XRD, selected area electron diffraction (SAED), and high-resolution transmission electron microscopy (HRTEM). The galvanostatic intermittent titration technique (GITT) analysis suggested that the Na ion diffusivity of LS-NFM has been significantly improved compared to the single-phased undoped NFM control. When cycled at a high current density of 100 mA g^{-1}, the LS-NFM cathode exhibited a first-cycle Coulombic efficiency of 88% and reversible capacity of 96 mAh g^{-1} after 100 cycles with the capacity retention of 86%. Structural characterization by *ex situ* soft and hard X-ray absorption spectroscopy (XAS) suggested that the capacity of LS-NFM largely resulted from the N^{2+}/Ni^{4+} redox couple and slightly from the Fe^{3+}/Fe^{4+} redox couple.

■ EXPERIMENTAL SECTION

Materials Synthesis. All of the chemicals were purchased from Sigma-Aldrich (purity ≥99%). LS-NFM was prepared by a solid state reaction of the coprecipitated precursor (Ni$_{0.4}$Fe$_{0.2}$Mn$_{0.4}$)C$_2$O$_4$, Li$_2$CO$_3$, and Na$_2$CO$_3$. For precursor synthesis, the stoichiometric amount of NiSO$_4$·6H$_2$O, FeSO$_4$·7H$_2$O, and MnSO$_4$·H$_2$O was dissolved in water and then added into the Na$_2$C$_2$O$_4$ solution. The solution was then kept at 70 °C for 3 h under stirring in air, and the resultant powder was filtered, washed, and dried in air at 105 °C.[10] The as-prepared precursor powder was grinded together with stoichiometric amounts of Li$_2$CO$_3$ and Na$_2$CO$_3$ for 1 h and then pressed into pellets. The pellets were heated at 500 °C for 8 h

followed by 800 °C for 8 h in a tube furnace under mixed oxygen/argon atmosphere (O_2:Ar = 1:4 v/v). Undoped $NaNi_{0.4}Fe_{0.2}Mn_{0.4}O_2$ (NFM) was also prepared by a solid state reaction of coprecipitated precursor $Ni_{1/2}Mn_{1/2}(OH)_2$, Fe_2O_3, and Na_2CO_3 for comparison.[17] The stoichiometric amounts of chemicals were grinded for 1 h and then pressed into pellets. The pellets were heated at 800 °C for 24 h in air. Both cathodes were transferred into glovebox immediately to avoid contact with moisture in the air.

Structural Characterizations. XRD patterns were obtained by a Rigaku Miniflex 600 with Cu Kα radiation (λ = 1.5418 Å), and powder samples were tested in a flat sample stage and scanned from 5° to 120° (2θ) at the rate of 0.8°/min and 0.01°/step. Then the structure was analyzed by the General Structure Analysis System (GSAS) package.[33] The cycled laminated electrodes were scanned in the range 10°−80° (2θ). The morphology of LS-NFM sample was characterized by a field-emission scanning electron microscope (FESEM, FEI Teneo) at an accelerating voltage of 15 kV. The TEM images were acquired by a JEOL 2100F with the accelerating voltage of 200 kV. TEM specimens of cycled samples were prepared in an Ar-filled dry glovebox (O_2 < 0.5 ppm). A Gatan vacuum transfer holder was employed to transfer the specimen from the glovebox to the microscope directly without exposure to air. The soft X-ray adsorption spectroscopy (XAS) measurements were performed at beamline 8-2 at the Stanford Synchrotron Radiation Lightsource (SSRL). Data were acquired under ultrahigh vacuum (10^{-9} Torr) conditions in a single load at room temperature, using total electron yield (TEY) via the drain current. Hard XAS measurements for the Ni, Fe, and Mn K-edge were performed at the Advanced Photon Source on beamline 5-BM-D in transmission mode. All the *ex situ* samples were harvested from the cycled cells, cleaned, and sealed with Kapton tape in Ar-filled dry glovebox. The samples were subjected to the measurements immediately after they were taken out from sealed containers. Extended X-ray absorption fine structure (EXAFS) data processing and analysis were performed using the IFEFFIT package.[34] The normalized EXAFS spectra were converted from energy to wave vector k and then weighted by k^3. The coordination number was fixed as 6 for the first-shell transition metal−oxygen (TM−O) and 6 for the second-shell transition metal−transition metal (TM−TM).

Electrochemical Characterizations. Both LS-NFM and NFM laminated electrodes were prepared by mixing 80% active materials, 10% super carbon C45 (Timcal America Inc.), and 10% poly-(vinylidene fluoride) (PVDF) and screen-printed on an aluminum current collector. The electrode was punched into a 1.5 cm diameter disc using a Precision Disc Cutter (MTI) with a loading density of ~2.7 mg cm^{-2}. The half-cells were prepared with LS-NFM or NFM cathode electrodes, glass fiber separator (Celgard), and sodium counter electrode in an electrolyte of 1 M $NaPF_6$ in propylene carbonate (PC). Both cathodes were cycled on an Arbin battery tester with the potential window of 2−4.2 V. GITT was conducted on a Maccor battery tester with the cell charged/discharged at a current density of 12 mA g^{-1} for a pulse of 30 min followed by a relaxation of 12 h to approach the steady state value where the voltage variation is <3 mV h^{-1}. All of the samples were precycled prior to GITT measurements.

RESULTS AND DISCUSSION

The LS-NFM is designed such that a mixed-phased O3/spinel structure can be formed. Specifically, the ratio between Na ion over the sum of Li and transition metal ions is adjusted to be below 1 as it has been shown that O3 phase may not form at high Na content.[27,35] In addition, the separate spinel phase is more favorable over the pure layered phase when the Li content is high. However, if the Li content is too high, it can lead to P2 phase evolution.[27] At the same time, we also need to consider that there are limited cation sites in the structure but sufficient Na source should be put to provide high capacity. Therefore, the final composition was designed as

$Na_{0.87}Li_{0.25}Ni_{0.4}Fe_{0.2}Mn_{0.4}O_{2+\delta}$, which was confirmed by ICP-MS.

The morphology of LS-NFM electrode is investigated by SEM. Figure S1 (Supporting Information) shows that the material is composed of plate-shaped particles. The XRD patterns of as-prepared LS-NFM and undoped NFM samples are presented in Figure 1 and Figure S2, respectively. Structural
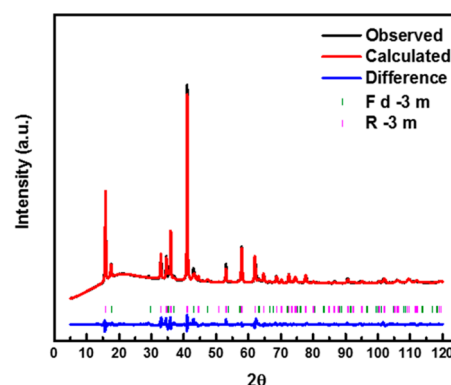

Figure 1. X-ray diffraction pattern and Rietveld refinement of the as-prepared LS-NFM powders.

parameters through Rietveld refinement are summarized in Table S1 (Supporting Information). The lattice parameters of LS-NFM were refined based on the rhombohedral α-$NaFeO_2$ structure (space group: $R\bar{3}m$) and cubic spinel structure (space group: $Fd\bar{3}m$) as the secondary phase. The calculated pattern is in good agreement with the experimental data where R_{wp} = 2.35% and R_p = 1.37%. The Rietveld refinement result suggests that the LS-NFM material is composed of 94% of a dominant α-$NaFeO_2$ phase with the lattice parameters of $a = b = 2.9550(2)$ Å and $c = 15.903(1)$ Å and 6% of a secondary spinel phase with $a = 8.1806(8)$ Å. For the XRD pattern of NFM, the single α-$NaFeO_2$ phase was refined with the lattice parameters of $a = b = 2.96894(4)$ Å and $c = 16.0119(4)$ Å. A slight lattice shrinkage along the z-axis was observed in the LS-NFM sample compared to the NFM sample, which may be due to partial oxidation of Ni^{2+} (0.69 Å) to Ni^{3+} (0.56 Å) because of the substitution of Li ions in the transition metal layer, and the result is consistent with a previous report.[23] Moreover, we conducted *ex situ* XRD on the as-prepared and first discharged (sodiated) laminated electrodes to investigate the structural evolution (Figure S3) upon cycling. The cycled samples were covered by Kapton tape to prevent exposure to air. Both XRD patterns showed a dominant O3-type layered structure with the secondary spinel phase. The asterisk-marked peaks at 18.29°, 43.77°, and 63.80° correspond to the (111), (400), and (511) planes of the spinel phase, respectively. In terms of the layered O3 phase, the (003) and (006) planes shifted to a higher angle after the first discharging process, suggesting a slight decrease in c. Because of the electrostatic attraction between Na^+ and O^{2-} ions, the decrease in c can be ascribed to a higher concentration of Na^+ ions into the layered structure, filling in the Na vacancies in the as-prepared sample (Table S1).[36]

The as-prepared, 1st discharged, and 50th discharged LS-NFM samples were also investigated by TEM (Figure 2). The HRTEM images are shown in Figures 2a, 2b, and 2c where the red and white dashed squares indicate the spinel and layered components, respectively, and the insets are the corresponding
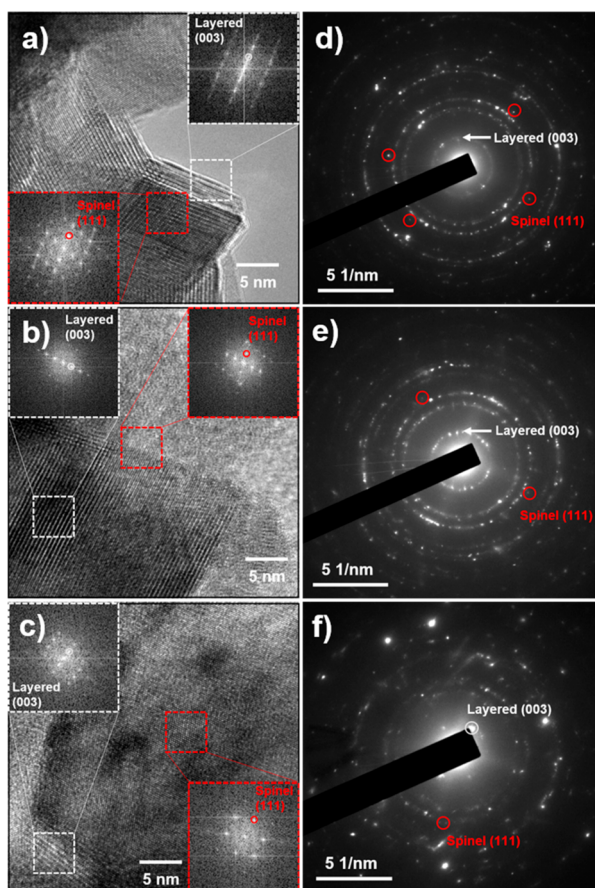
Figure 2. HRTEM images of (a) as-prepared, (b) 1st discharged, and (c) 50th discharged LS-NFM sample. The red and white dashed squares indicate the spinel and layered components, respectively, where the corresponding FFT images are shown as insets. The red and white circles indicate the spinel (111) plane with the zone axis [110] and layered (003) plane with the zone axis [100], respectively. SAED images of (d) as-prepared, (e) 1st discharged, and (f) 50th discharged LS-NFM sample where the red circles and white arrows or circle indicate the planes from spinel and layered phase, respectively.

fast Fourier transform (FFT) images. The HRTEM image of the as-prepared LS-NFM sample (Figure 2a) exhibits the (003) plane of the layered phase and the (111) plane of the spinel phase where nanoscale domains of the layered and spinel components are structurally integrated. It is worth noting the great structural compatibility and connectivity of the two close-packed structures.[37] After the first discharge, the close-packed layered and spinel phase in LS-NFM sample remain in the structure (Figure 2b), which is consistent with the *ex situ* XRD results (Figure S3). Note that after 50 cycles the layered and spinel structure still preserve (Figure 2c), suggesting the great structural reversibility and stability. The SAED images of the as-prepared, 1st discharged, and 50th discharged LS-NFM sample are shown in Figures 2d, 2e, and 2f, respectively, where the red circles and white arrows indicate planes from the spinel and layered phase, respectively. The SAED pattern of the as-prepared LS-NFM displays a dominant polycrystalline layered O3-type structure and the minor spinel phase, consistent with the XRD result that the LS-NFM cathode contains a large amount of layered structure (94%) and a small fraction of the spinel phase (6%). The existence of the spinel phase in the 1st discharged sample (Figure 2e) as

well as the 50th discharged sample (Figure 2f) suggests good structural stability of the LS-NFM cathode.

The voltage profiles of LS-NFM and NFM electrodes cycled with a potential window of 2−4.2 V at 12 mA g^{-1} are presented in Figures 3a and 3b, respectively. The correspond-
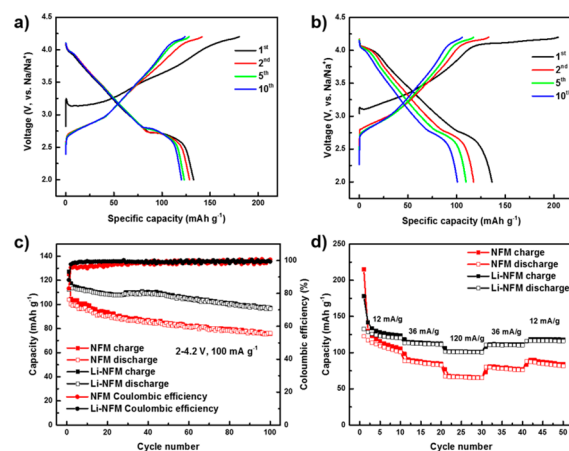

Figure 3. Voltage profiles of (a) LS-NFM and (b) NFM cathode cycled at a current rate of 12 mA g^{-1}. (c) Cycling performance and (d) rate capability of LS-NFM and NFM cathode.

ing dQ/dV plots are shown in Figure S4. Both cathodes have a similar plateau region during charging (∼2.75−2.9 V) and discharging (2.8−2.5 V) processes, which correspond to the reversible phase transitions between O3 and P3 phases.[18,20,38−41] In addition, both cathodes exhibit a plateau at ∼4.16 V (Figures 2a and 2b) as can be also indicated by the oxidation peak in the dQ/dV plots (Figure S4) during the charging process, which could be associated with the phase transition from P3 to O3′ (also known as O3 phase at high voltage).[20,38,39] Moreover, side reactions with electrolyte, formation of solid electrolyte interphase (SEI), and/or polarization may also contribute the plateau at high voltage.[42−44] For the discharging process of NFM cathode, a distinct plateau at 3.9−4.1 V gradually became sloping after 10 cycles, and the corresponding peak intensity in the dQ/dV plot significantly decreased (Figure S4), which can be attributed to the irreversible transition from O3′ to P3 phase[20] and/or detrimental coinsertion of solvent in the electrolyte at high voltages.[18,45] On the other hand, the plateau at ∼4.16 V of the LS-NFM cathode is maintained for subsequent cycles (Figure S4) during the discharging process, suggesting a reversible phase transition. The sloping profiles between the plateaus at higher and lower voltages for both cathodes could be related to a solid−solution reaction with P3 structure.[18] The first charge capacity of LS-NFM and NFM is 180 and 205 mAh g^{-1}, respectively, and the first-cycle Coulombic efficiency of LS-NFM cathode (73%) has been significantly enhanced compared to the NFM cathode (52%), which is possibly due to the structural stabilization by the spinel phase in the mixed phased LS-NFM cathode. Although the Coulombic efficiency has been improved in LS-NFM cathode, it is not high possibly due to the irreversible side reaction at the surface or the formation of SEI at high upper cutoff potential (4.2 V).[2,46,47]

We have studied the cycling performance of both LS-NFM and NFM electrodes (Figure 3c) at a current rate of 100 mA g^{-1}. The first discharge capacity of NFM (104 mAh g^{-1}) is much smaller than that of LS-NFM (112 mAh g^{-1}). Moreover,

LS-NFM exhibits a higher discharge capacity and capacity retention (96 mAh g^{-1}, 86%) than the NFM control (75 mAh g^{-1}, 70%) after 100 cycles, indicating a significantly improved cycling performance of LS-NFM cathode. The first-cycle Coulombic efficiency of LS-NFM is 88% and approaches 99% after five cycles, much faster than the NFM cathode, which reaches 99% Coulombic efficiency after 28 cycles. The improved Coulombic efficiency is possibly due to the unique design of LS-NFM cathode with the intergrown spinel phase stabilizing the layered structure.

One of the advantages of the layered spinel cathodes used for lithium ion batteries is the enhanced rate capability due to the shortened diffusion path that is created by the integration of 3D channels (spinel phase) and 2D channels (layered phase).[48,49] We also investigated the rate capability of our layered spinel cathode for sodium ion batteries (Figure 3d). Both LS-NFM and NFM cathodes were cycled at the rate of 12, 36, 120, and 36 mA g^{-1} and back to 12 mA g^{-1}. The LS-NFM cathode delivered 129 mAh g^{-1} at 12 mA g^{-1} and 101 mAh g^{-1} at 120 mA g^{-1}. When cycled back to the low current rate of 12 mA g^{-1}, it delivered a capacity of 118 mAh g^{-1}, with a 92% capacity retention. In contrast, the NFM cathode delivered 106 and 66 mAh g^{-1} in capacity at the initial rates of 12 and 120 mA g^{-1}. It exhibited a capacity of 84 mAh g^{-1} when cycled back to the low rate of 12 mA g^{-1}, with an 80% capacity retention. The LS-NFM electrode exhibited a better rate capability and capacity retention compared to the NFM electrode.

The improved rate capability in LS-NFM electrode suggests faster charge transport kinetics within the LS-NFM cathode; thus, we conducted GITT to investigate the Na$^+$ diffusion coefficient of cycled LS-NFM and NFM electrodes (Figure 4a). The plot of Na$^+$ diffusivity as a function of voltage during the charge and discharge process is shown in Figures 4b and 4c, respectively. (Details of GITT analysis can be found in the Supporting Information.) At the beginning of the charging process, the diffusion coefficient of LS-NFM (2.4×10^{-13} cm^2 s^{-1} at 2.67 V) is about 1 order of magnitude higher than that of NFM (1.44×10^{-14} cm^2 s^{-1} at 2.80 V), and the diffusivity of LS-NFM surpasses that of the NFM cathode until the electrodes are charged to 3.75 V. Moreover, the diffusivity of LS-NFM electrode during discharge process is also ~1 order of magnitude higher than that of the NFM electrode throughout the whole potential window. The LS-NFM electrode exhibits a faster Na$^+$ diffusivity in both charge and discharge processes compared to the NFM electrode. This result is in good agreement with the rate capability study discussed above. The improved Na$^+$ diffusivity in LS-NFM is possibly due to the 3D diffusion channels from the spinel structure that provide direct connectivity between layered and spinel components, which greatly shorten the ion diffusion distance. This hypothesis has been investigated in layered spinel cathode materials for lithium ion batteries.[48,50−52] The diffusion coefficients of LS-NFM drop when the voltage is near 2.82 V, and recover at 2.93 V, which can be explained by the phase transformation between O3 and P3 phases,[18] consistent with the plateau region in the voltage profile (Figure 3a). This implies the O3−P3 phase transformation is a diffusion-controlled process associated with the complex Na ion/vacancy ordering and host rearrangement.[53] At the region of 2.93−3.63 V, the diffusion coefficients in both LS-NFM and NFM electrodes remain stable, indicating a relatively low barrier of Na ion extraction from the host materials. When the electrodes are charged
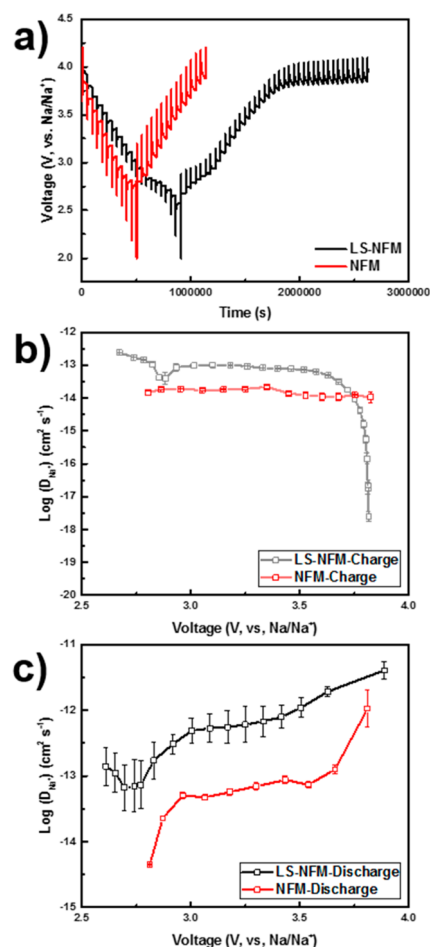

Figure 4. (a) GITT profile and Na$^+$ diffusivity as a function of voltage of LS-NFM and NFM cathodes in (b) charge and (c) discharge process.

above 3.63 V, the significant decrease of the diffusion coefficient of LS-NFM can be ascribed to the sluggish phase transformation from the P3 to O3′ phase, which was observed in *in situ* XRD studies elsewhere.[20,38] On the other hand, the decrease of diffusion coefficient at high voltage is not observed in the NFM cathode, possibly due to the irreversible P3−O3′ phase transition during the initial cycle. Indeed, the long plateau at ~4.16 V during the first charge (Figure 2b) becomes sloping after first cycle and the corresponding peak intensity in dQ/dV (Figure S4) significantly decreases, both of which suggest the irreversible P3−O3′ phase transition in NFM electrode.

The *ex situ* XAS was conducted to explore the chemical environment of transition metals at various states of charge (SOC) including pristine, charged to 4.0 V, charged to 4.2 V, discharged to 2.4 V, and discharged to 2.0 V (Figure 5). X-ray absorption near-edge structure (XANES) spectra at Ni, Mn, and Fe K-edges are shown in Figures 5a, 5b, and 5c, respectively. The onset of the transition metal k-edge is resulted from the symmetry-allowed transitions from the 1s core electron to excited vacant bound states.[54] The pre-edge absorption is formally electric dipole-forbidden transition of a 1s electron to an unoccupied 3d orbital.[54,55] The first strong absorption in the low-energy region corresponds to a shakedown process originally, from the ligand-to-metal charge transfer (LMCT).[48,56] The main absorption edge is due to the
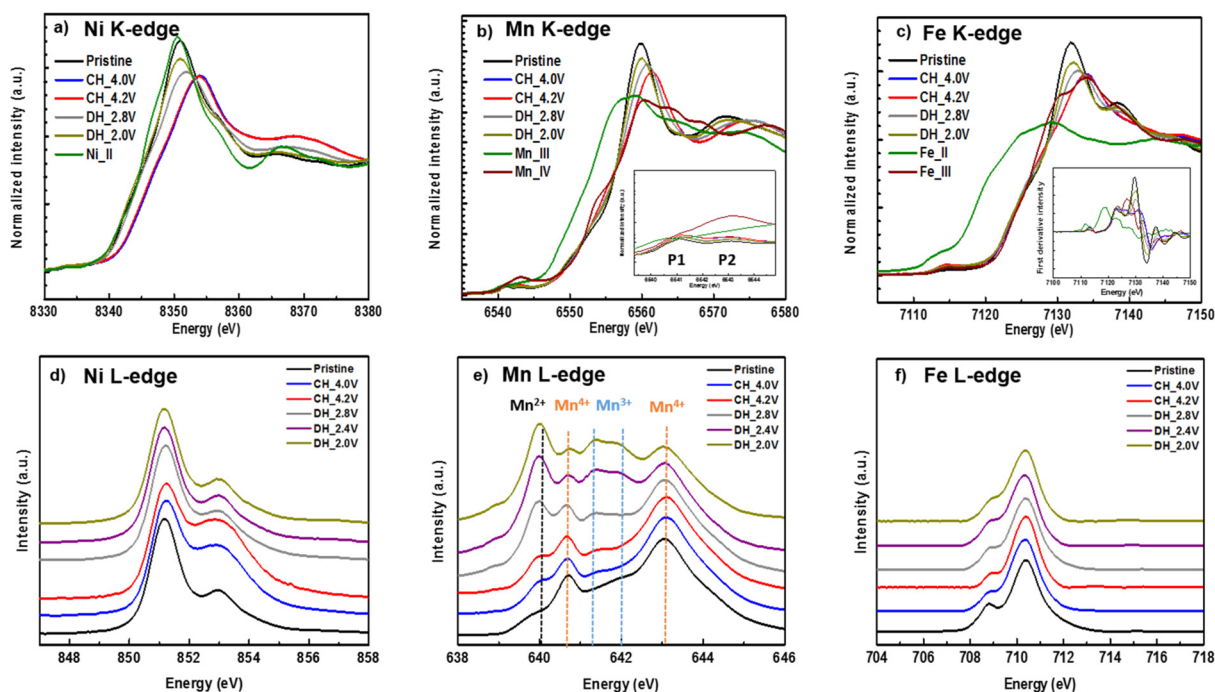
Figure 5. *Ex situ* (a) Ni, (b) Mn, and (c) Fe K-edge XANES spectra of LS-NFM electrode at different SOCs during the first charging and discharging process. The inset in (b) shows the pre-edge features of Mn K-edge spectra of samples at different SOCs where P1 and P2 correspond to transitions from 1s to 3de$_g$ and 3dt$_{2g}$ with a weak crystal field, respectively. The inset in (c) shows the first-derivative curves of the original data. *Ex situ* (d) Ni, (e) Mn, and (f) Fe L-edge sXAS spectra of LS-NFM electrode at different SOCs during the first charging and discharging process. The data were recorded under the TEY mode.

electric dipole allowed transition from a 1s to a 4p state.[54,55,57] The Ni K-edge spectra of the pristine sample and the NiO standard closely resemble each other, indicating the existence of Ni^{2+}. A significant shift of the edge to higher energy is observed during the charge process, suggesting the oxidation of Ni^{2+} ions during the extraction of Na^+ ions. The Ni K-edge spectra gradually shift back to the pristine low-energy region during discharge process, suggesting the reversible reduction of high oxidation state Ni ions back to Ni^{2+}. The edge position of the Mn K-edge spectrum of the pristine LS-NFM sample is similar to that of the MnO_2 standard, indicating the pristine sample contains tetravalent Mn ions. As the Na ions are (de)intercalated, the shape of Mn K-edge spectra changes due to the changes in the Mn local environment but there is not a rigid shift to higher energy. A small shift of edge position during charge and discharge process is observed, which is consistent with a previous study of NFM (Na-$Ni_{0.25}Fe_{0.5}Mn_{0.25}O_2$) electrode.[58] Because it is very difficult to oxidize Mn^{4+} to a higher valence state electrochemically, the small shift can be presumably attributed to the change of the local structure of manganese coordination.[45,59] The Figure 5b inset shows the pre-edge features of Mn K-edge spectra of samples at different states of charge (SOC) where P1 and P2 correspond to transitions from 1s to 3de$_g$ and 3dt$_{2g}$ with a weak crystal field, respectively. A very subtle increase in intensity confirms the negligible valence change of Mn ions. The oxidation state of Fe ions can be determined by the inflection point of the Fe K-edge spectra, which is indicated by the peak maxima in the first-derivative curve (Figure 5c inset).[60,61] The inflection points of the pristine, 4.3 V-charged, and 2.0 V-discharged samples locate at 7129.8, 7131.4, and 7130.0 eV, respectively. A small shift of the inflection points to higher energy when charged above 4.0 V indicates that the Fe

ions are slightly oxidized. When discharged back to 2.0 V, the peak maxima shifted back to the position of pristine sample, suggesting a reversible Fe ion redox reaction, consistent with a previous study.[39] In summary, in this layered spinel cathode material, nickel is the dominant electrochemical redox species and largely contributes to the specific capacity along with minor contribution from Fe.

In addition to the investigation of the chemical state in the bulk material, soft XAS (sXAS) is used to probe chemical environments at the surface with depth sensitivities. The incident X-rays are absorbed by the sample through excitation of core-level electrons to unoccupied states above the vacuum or Fermi level.[62,63] The total electron yield (TEY) accounts for all the electrons escaping from the surface of the material and is measured by the net current that flows into the sample to neutralize the positively charged sample by escaped electrons.[64] The probing depth of TEY mode is approximately 2−5 nm due to the mean free path of electrons in the sample, largely representing the surface environment of examined materials.[62] Figure 5d shows the TEY mode of Ni L3 edge of the LS-NFM samples. The splitting of the edge can be attributed to the Ni 2p-Ni 3d electrostatic interaction and crystal field effect.[65] The integrated peak ratio of split edge at high energy ($L3_{high}$) over low energy ($L3_{low}$) has a positive relation with the oxidation state of nickel.[65] The split edge ratio of pristine, 4.0 V-charged, and 4.3 V-charged sample are 0.56, 1.73, and 2.22, respectively, suggesting the cathode is gradually oxidized during the charging process, while during the discharging process, the ratios of 2.8 V-discharged, 2.4 V-discharged, and 2.0 V-discharged states are 0.90, 0.58, and 0.56, respectively, suggesting the reduction of Ni ions. The ratio of pristine and fully discharged samples are both 0.56, suggesting great reversibility of the Ni redox couple. The TEY
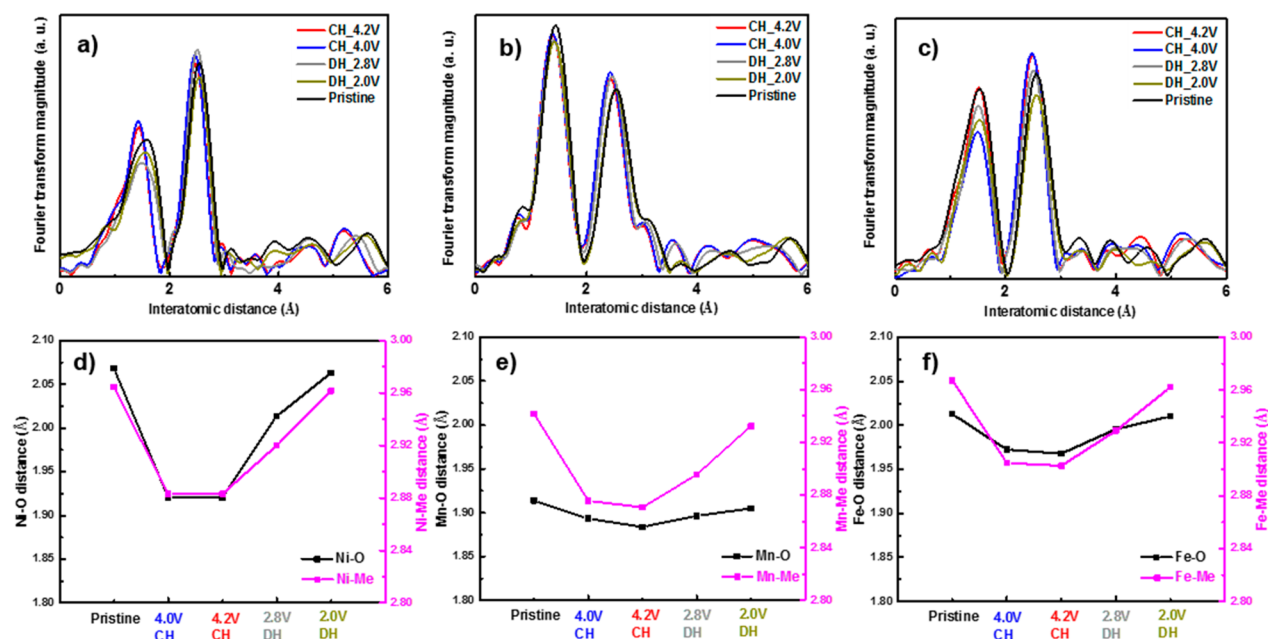
Figure 6. *Ex situ* Fourier transformed (a) Ni, (b) Mn, and (c) Fe K-edge EXAFS spectra of LS-NFM electrode at different SOCs during the first charging and discharging process. Simulated TM-TM and TM-O distances of (d) Ni, (e) Mn, and (f) Fe.

mode spectra of Mn L3 edge of the *ex situ* samples are also shown in Figure 5e. The peak at 640 eV corresponds to Mn^{2+} ions, the peak at 641.36 and 641.97 eV to Mn^{3+} ions, and the peak at 640.71 and 643.05 eV to Mn^{4+} ions, as illustrated by the dashed lines.[56,66] The pristine sample shows dominant Mn^{4+} ions in the structure. Little change is observed during the charging process to 4.2 V. However, a significant amount of Mn^{4+} ions are reduced to Mn^{3+} and Mn^{2+} ions when discharged to 2.8 V. The reduction of Mn^{4+} ions continued during the discharging process to 2.0 V. Note that in the traditional O3-type layered NFM cathode (Na-$Ni_{0.25}Fe_{0.5}Mn_{0.25}O_2$) the Mn^{4+} ion in the bulk is not electrochemically active during both charging and discharging processes.[58] However, Mn^{4+} ions possibly react with trace amount of moisture in the electrode–electrolyte interface, leading to the slight reduction of Mn^{4+} ions to Mn^{3+} ions, which has been observed in a previous study of a single-phased R−3m Li-doped NFM cathode (Na-$[Li_{0.05}(Ni_{0.25}Fe_{0.25}Mn_{0.5})_{0.95}]O_2$) where a small shift during the charging process from Mn^{4+} to Mn^{3+} ions was observed by XPS.[23] In the layered spinel cathode, a small amount of Mn^{2+} ions are generated during the charging process, presumably indicating that Mn^{4+} ions are first reduced to Mn^{3+} ions, followed by the disproportionate reaction $2Mn^{3+} = Mn^{2+} + Mn^{4+}$ of the specific and particular spinel composition at the electrode surface.[67] This reaction might form a surface layer, blocking the insertion of the solvent molecules and/or electrolyte anions into the layered structure, and therefore enhance the structural stability.[18,45] Furthermore, a reduction of Mn^{4+} ions to Mn^{3+} and Mn^{2+} ions is observed during the discharging process. As for the Fe L3-edge, the ratio of split edge at high energy over low energy has a positive relation with the oxidation state of iron.[68] The ratio of integrated intensity at high energy over that at low energy increases from the pristine to charged-4.0 V sample, suggesting Fe ions are oxidized when charged above 4.0 V, consistent with the XANES result (Figure 5c) and the practical first charge capacity (Figure 3a).

We have also examined the local structural evolution of LS-NFM cathode by hard X-ray EXAFS spectra. Figures 6a, 6b, and 6c show the Fourier transform magnitudes of Ni, Mn, and Fe K-edge spectra, respectively. The first intense peak is attributed to the TM−O coordination shell, and the second is the TM−TM shell. The quantitative fitting of EXAFS spectra shown in Figures 6d, 6e, and 6f (fitting details are provided in Table S2) provides the distances of TM−O and TM−TM bonds. For the pristine sample, the distances of Ni−O, Mn−O, and Fe−O are 2.07, 1.91, and 2.02 Å, respectively, consistent with the Shannon's ionic radii where the distance of Ni^{II}−O, Mn^{IV}−O, and Fe^{III}−O are 2.09, 1.93, and 2.01 Å, respectively, suggesting the good fitting of EXAFS spectra.[26,69] The distance of Ni−TM, Mn−TM, and Fe−TM are comparable to each other, indicating the uniform distribution of Ni, Mn, and Fe ions. When charged to 4.0 V, the Ni−O distance significantly decreases to 1.92 Å, and the Fe−O distance slightly decreases to 1.97 Å, suggesting the oxidation of Ni and Fe ions. However, the negligible decrease in Mn−O distance indicates the change of local environment of Mn ion but not the change of oxidation state. Therefore, we conclude that Ni redox couple contributed to most of capacity in the LS-NFM cathode. When discharged at 2.0 V, the distances of Ni−O, Mn−O, and Fe−O return to 2.06, 1.90, and 2.01 Å, respectively, suggesting the good reversibility of all redox pairs. Moreover, all of the TM−TM distances decrease when the sample is charged above 4.0 V, which is probably due to the decrease of the lattice parameter corresponding to the in-plane interatomic distance.[45] When discharged to 2.0 V, all of the TM−TM distances reversibly increased. In summary, the EXAFS results exhibit the reversible evolution of both redox couple and crystal structure of the LS-NFM cathode, which is determined by the evolution of TM−O and TM−TM bonding length that decreases during charging process and reversibly increases during discharging process. This reversible evolution presumably is resulted from the intergrowth of spinel and layered phase that stabilized the crystal structure above 4.0 V.

CONCLUSION

We successfully prepared a layered spinel cathode material for sodium ion batteries by Li substitution. In the traditional Li-substituted cathode, Li ions are located at the transition metal sites and form a single phase. However, we prepared a mixed-phased layered spinel cathode by increasing the Li stoichiometry. The Rietveld refinement on the XRD pattern suggests that the as-prepared material is composed of a 94% dominant O3-type layered phase and 6% secondary spinel phase. The HRTEM results show the remarkable structural compatibility and connectivity of the two components, indicating an intergrowth structure. In terms of the electrochemical performance, both cycling stability and rate capability have been significantly improved in the LS-NFM cathode compared to the undoped NFM control. It maintains a discharge capacity retention of 86% after 100 cycles at a current rate of 100 mA g^{-1} in a potential window of 2−4.2 V, which is much better than that of the NFM control (70% capacity retention). The diffusion coefficient of LS-NFM is 1 order of magnitude higher than that of the NFM at the beginning of the charging process. Moreover, the diffusivity of LS-NFM during discharge process is also ~1 order of magnitude higher than that of NFM sample throughout the whole potential window. It explains the superior rate capability of the LS-NFM electrode. The enhanced charge transport kinetics can be explained by the improved ion diffusion through direct channels between the 2D layered and 3D spinel component. The voltage profile of LS-NFM shows a reversible plateau above 4.0 V while the high voltage plateau of the NFM cathode is irreversible, suggesting the enhanced structural and electrochemical stability of LS-NFM cathode by the addition of the spinel phase. We further investigated the origin of the enhanced electrochemical performance in the LS-NFM cathode by *ex situ* XAS. Both hard/soft XAS results suggest that Ni^{2+}/Ni^{4+} and Fe^{3+}/Fe^{4+} redox couples are electrochemically active while the Ni^{2+}/Ni^{4+} redox couple contributes to most of the capacity in the LS-NFM cathode. Moreover, the XAS results suggest great reversibility of the redox pairs and crystal structure, which presumably is associated with the intergrowth of spinel and layered phase that stabilized the crystal structure above 4.0 V. In addition to the substitution of various transition metals or the modification of the stoichiometry of each transition metal, this study provides a new strategy to improve electrochemical performance of layered cathode materials for sodium ion batteries.

ASSOCIATED CONTENT

Ⓢ Supporting Information

The Supporting Information is available free of charge on the ACS Publications website at DOI: 10.1021/acs.chemmater.8b02614.

Morphology of LS-NFM cathode, Rietveld refinement results of LS-NFM and NFM cathode, details of GITT and EXAFS (PDF)

AUTHOR INFORMATION

Corresponding Authors

*H.X: E-mail, clairexiong@boisestate.edu.
*J.X.: E-mail, jingxulbl@gmail.com.

ORCID Ⓞ

Wei Tong: 0000-0002-2878-1297

Hui Xiong: 0000-0003-3126-1476

REFERENCES

(1) Yabuuchi, N.; Kubota, K.; Dahbi, M.; Komaba, S. Research Development on Sodium-Ion Batteries. *Chem. Rev.* **2014**, *114* (23), 11636−11682.
(2) Pan, H. L.; Hu, Y. S.; Chen, L. Q. Room-temperature stationary sodium-ion batteries for large-scale electric energy storage. *Energy Environ. Sci.* **2013**, *6* (8), 2338−2360.
(3) Kundu, D.; Talaie, E.; Duffort, V.; Nazar, L. F. The Emerging Chemistry of Sodium Ion Batteries for Electrochemical Energy Storage. *Angew. Chem., Int. Ed.* **2015**, *54* (11), 3431−3448.
(4) Slater, M. D.; Kim, D.; Lee, E.; Johnson, C. S. Sodium-Ion Batteries. *Adv. Funct. Mater.* **2013**, *23* (8), 947−958.
(5) Kim, S.-W.; Seo, D.-H.; Ma, X.; Ceder, G.; Kang, K. Electrode Materials for Rechargeable Sodium-Ion Batteries: Potential Alternatives to Current Lithium-Ion Batteries. *Adv. Energy Mater.* **2012**, *2* (7), 710−721.
(6) Slater, M. D.; Kim, D.; Lee, E.; Johnson, C. S. Sodium-Ion Batteries. *Adv. Funct. Mater.* **2013**, *23* (8), 947−958.
(7) Ellis, B. L.; Nazar, L. F. Sodium and sodium-ion energy storage batteries. *Curr. Opin. Solid State Mater. Sci.* **2012**, *16* (4), 168−177.
(8) Xu, J.; Lee, D. H.; Meng, Y. S. Recent Advanced in Sodium Intercalation Positive Electrode Materials for Sodium Ion Batteries. *Funct. Mater. Lett.* **2013**, *6* (1), 1330001.
(9) Grosjean, C.; Miranda, P. H.; Perrin, M.; Poggi, P. Assessment of world lithium resources and consequences of their geographic distribution on the expected development of the electric vehicle industry. *Renewable Sustainable Energy Rev.* **2012**, *16* (3), 1735−1744.
(10) Ryu, W. H.; Nam, D. H.; Ko, Y. S.; Kim, R. H.; Kwon, H. S. Electrochemical performance of a smooth and highly ordered TiO$_2$ nanotube electrode for Li-ion batteries. *Electrochim. Acta* **2012**, *61*, 19−24.
(11) Martin, G.; Rentsch, L.; Höck, M.; Bertau, M. Lithium market research − global supply, future demand and price development. *Energy Storage Mater.* **2017**, *6*, 171−179.

(12) Speirs, J.; Contestabile, M.; Houari, Y.; Gross, R. The future of lithium availability for electric vehicle batteries. *Renewable Sustainable Energy Rev.* **2014**, *35*, 183−193.

(13) Vikström, H.; Davidsson, S.; Höök, M. Lithium availability and future production outlooks. *Appl. Energy* **2013**, *110*, 252−266.

(14) Palomares, V.; Serras, P.; Villaluenga, I.; Hueso, K. B.; Carretero-Gonzalez, J.; Rojo, T. Na-ion batteries, recent advances and present challenges to become low cost energy storage systems. *Energy Environ. Sci.* **2012**, *5* (3), 5884−5901.

(15) Kubota, K.; Yabuuchi, N.; Yoshida, H.; Dahbi, M.; Komaba, S. Layered oxides as positive electrode materials for Na-ion batteries. *MRS Bull.* **2014**, *39* (5), 416−422.

(16) Zhao, J.; Zhao, L. W.; Dimov, N.; Okada, S.; Nishida, T. Electrochemical and Thermal Properties of alpha-NaFeO2 Cathode for Na-Ion Batteries. *J. Electrochem. Soc.* **2013**, *160* (5), A3077−A3081.

(17) Yabuuchi, N.; Yano, M.; Yoshida, H.; Kuze, S.; Komaba, S. Synthesis and Electrode Performance of O3-Type NaFeO2-NaNi1/2Mn1/2O2 Solid Solution for Rechargeable Sodium Batteries. *J. Electrochem. Soc.* **2013**, *160* (5), A3131−A3137.

(18) Yuan, D. D.; Wang, Y. X.; Cao, Y. L.; Ai, X. P.; Yang, H. X. Improved Electrochemical Performance of Fe-Substituted NaNi0.5Mn0.5O2 Cathode Materials for Sodium-Ion Batteries. *ACS Appl. Mater. Interfaces* **2015**, *7* (16), 8585−8591.

(19) Wang, H.; Liao, X. Z.; Yang, Y.; Yan, X. M.; He, Y. S.; Ma, Z. F. Large-Scale Synthesis of NaNi1/3Fe1/3Mn1/3O2 as High Perform-ance Cathode Materials for Sodium Ion Batteries. *J. Electrochem. Soc.* **2016**, *163* (3), A565−A570.

(20) Li, X.; Wu, D.; Zhou, Y. N.; Liu, L.; Yang, X. Q.; Ceder, G. O3-type Na(Mn0.25Fe0.25Co0.25Ni0.25)O2: A quaternary layered cathode compound for rechargeable Na ion batteries. *Electrochem. Commun.* **2014**, *49*, 51−54.

(21) Yabuuchi, N.; Kajiyama, M.; Iwatate, J.; Nishikawa, H.; Hitomi, S.; Okuyama, R.; Usui, R.; Yamada, Y.; Komaba, S. P2-type Nax[Fe1/2Mn1/2]O2 made from earth-abundant elements for rechargeable Na batteries. *Nat. Mater.* **2012**, *11*, 512−517.

(22) Zhang, S. M.; Liu, Y.; Zhang, N.; Zhao, K.; Yang, J. H.; He, S. Y. O3-type NaNi0.33Li0.11Ti0.56O2-based electrode for symmetric sodium ion cell. *J. Power Sources* **2016**, *329*, 1−7.

(23) Oh, S. M.; Myung, S. T.; Hwang, J. Y.; Scrosati, B.; Amine, K.; Sun, Y. K. High Capacity O3-Type Na[Li-0.05(Ni0.25Fe0.25Mn0.5)(0.95)]O2 Cathode for Sodium Ion Batteries. *Chem. Mater.* **2014**, *26* (21), 6165−6171.

(24) Zheng, S. Y.; Zhong, G. M.; McDonald, M. J.; Gong, Z. L.; Liu, R.; Wen, W.; Yang, C.; Yang, Y. Exploring the working mechanism of Li+ in O3-type NaLi0.1Ni0.35Mn0.55O2 cathode materials for rechargeable Na-ion batteries. *J. Mater. Chem. A* **2016**, *4* (23), 9054−9062.

(25) Xu, J.; Liu, H. D.; Meng, Y. S. Exploring Li substituted O3-structured layered oxides NaLixNi1/3-xMn1/3+xCo1/3-xO2 (x = 0.07, 0.13, and 0.2) as promising cathode materials for rechargeable Na batteries. *Electrochem. Commun.* **2015**, *60*, 13−16.

(26) Shannon, R. D. Revised Effective Ionic-Radii and Systematic Studies of Interatomic Distances in Halides and Chalcogenides. *Acta Crystallogr., Sect. A: Cryst. Phys., Diffr., Theor. Gen. Crystallogr.* **1976**, *32* (Sep1), 751−767.

(27) Lee, E.; Lu, J.; Ren, Y.; Luo, X. Y.; Zhang, X. Y.; Wen, J. G.; Miller, D.; DeWahl, A.; Hackney, S.; Key, B.; Kim, D.; Slater, M. D.; Johnson, C. S. Layered P2/O3 Intergrowth Cathode: Toward High Power Na-Ion Batteries. *Adv. Energy Mater.* **2014**, *4* (17), 1400458.

(28) Chen, X. Q.; Zhou, X. L.; Hu, M.; Liang, J.; Wu, D. H.; Wei, J. P.; Zhou, Z. Stable layered P3/P2 Na0.66Co0.5Mn0.5O2 cathode materials for sodium-ion batteries. *J. Mater. Chem. A* **2015**, *3* (41), 20708−20714.

(29) Bianchini, M.; Gonzalo, E.; Drewett, N. E.; Ortiz-Vitoriano, N.; del Amo, J. M. L.; Bonilla, F. J.; Acebedo, B.; Rojo, T. Layered P2-O3 sodium-ion cathodes derived from earth abundant elements. *J. Mater. Chem. A* **2018**, *6* (8), 3552−3559.

(30) Gao, G.; Tie, D.; Ma, H.; Yu, H.; Shi, S.; Wang, B.; Xu, S.; Wang, L.; Zhao, Y. Interface-rich mixed P2 + T phase NaxCo0.1Mn0.9O2 (0.44 [less-than-or-equal] x [less-than-or-equal] 0.7) toward fast and high capacity sodium storage. *J. Mater. Chem. A* **2018**, *6* (15), 6675−6684.

(31) Liu, X. Z.; Wang, X.; Iyo, A.; Yu, H. J.; Li, D.; Zhou, H. S. High stable post-spinel NaMn2O4 cathode of sodium ion battery. *J. Mater. Chem. A* **2014**, *2* (36), 14822−14826.

(32) Ling, C.; Mizuno, F. Phase Stability of Post-spinel Compound AMn(2)O(4) (A = Li, Na, or Mg) and Its Application as a Rechargeable Battery Cathode. *Chem. Mater.* **2013**, *25* (15), 3062−3071.

(33) Larson, A. C.; Von Dreele, R. B. *General Structure Analysis System (GSAS)*; Los Alamos National Laboratory: Los Alamos, NM, 2004.

(34) Newville, M. IFEFFIT: interactive XAFS analysis and FEFF fitting. *J. Synchrotron Radiat.* **2001**, *8* (2), 322−324.

(35) Clément, R. J.; Bruce, P. G.; Grey, C. P. Review—Manganese-Based P2-Type Transition Metal Oxides as Sodium-Ion Battery Cathode Materials. *J. Electrochem. Soc.* **2015**, *162* (14), A2589−A2604.

(36) Wang, X. F.; Liu, G. D.; Iwao, T.; Okubo, M.; Yamada, A. Role of Ligand-to-Metal Charge Transfer in O3-Type NaFeO2-NaNiO2 Solid Solution for Enhanced Electrochemical Properties. *J. Phys. Chem. C* **2014**, *118* (6), 2970−2976.

(37) Nayak, P. K.; Grinblat, J.; Levi, M.; Levi, E.; Zitoun, D.; Markovsky, B.; Aurbach, D. Studies of a layered-spinel Li[Ni1/3Mn2/3]O-2 cathode material for Li-ion batteries synthesized by a hydrothermal precipitation. *Mater. Sci. Eng., B* **2016**, *213*, 131−139.

(38) Li, X.; Wang, Y.; Wu, D.; Liu, L.; Bo, S. H.; Ceder, G. Jahn-Teller Assisted Na Diffusion for High Performance Na Ion Batteries. *Chem. Mater.* **2016**, *28* (18), 6575−6583.

(39) Xie, Y. Y.; Wang, H.; Xu, G. L.; Wang, J. J.; Sheng, H. P.; Chen, Z. H.; Ren, Y.; Sun, C. J.; Wen, J. G.; Wang, J.; Miller, D. J.; Lu, J.; Amine, K.; Ma, Z. F. In Operando XRD and TXM Study on the Metastable Structure Change of NaNi1/3Fe1/3Mn1/3O2 under Electrochemical Sodium-Ion Intercalation. *Adv. Energy Mater.* **2016**, *6* (24), 1601306.

(40) Sathiya, M.; Hemalatha, K.; Ramesha, K.; Tarascon, J. M.; Prakash, A. S. Synthesis, Structure, and Electrochemical Properties of the Layered Sodium Insertion Cathode Material: NaNi1/3Mn1/3Co1/3O2. *Chem. Mater.* **2012**, *24* (10), 1846−1853.

(41) Lei, Y. C.; Li, X.; Liu, L.; Ceder, G. Synthesis and Stoichiometry of Different Layered Sodium Cobalt Oxides. *Chem. Mater.* **2014**, *26* (18), 5288−5296.

(42) Park, Y.; Shin, S. H.; Hwang, H.; Lee, S. M.; Kim, S. P.; Choi, H. C.; Jung, Y. M. Investigation of solid electrolyte interface (SEI) film on LiCoO2 cathode in fluoroethylene carbonate (FEC)-containing electrolyte by 2D correlation X-ray photoelectron spectroscopy (XPS). *J. Mol. Struct.* **2014**, *1069*, 157−163.

(43) Balasubramanian, M.; Lee, H. S.; Sun, X.; Yang, X. Q.; Moodenbaugh, A. R.; McBreen, J.; Fischer, D. A.; Fu, Z. Formation of SEI on cycled lithium-ion battery cathodes - Soft X-ray absorption study. *Electrochem. Solid-State Lett.* **2002**, *5* (1), A22−A25.

(44) Yang, L.; Ravdel, B.; Lucht, B. L. Electrolyte Reactions with the Surface of High Voltage LiNi0.5Mn1.5O4 Cathodes for Lithium-Ion Batteries. *Electrochem. Solid-State Lett.* **2010**, *13* (8), A95−A97.

(45) Komaba, S.; Yabuuchi, N.; Nakayama, T.; Ogata, A.; Ishikawa, T.; Nakai, I. Study on the Reversible Electrode Reaction of Na1-xNi0.5Mn0.5O2 for a Rechargeable Sodium-Ion Battery. *Inorg. Chem.* **2012**, *51* (11), 6211−6220.

(46) Chagas, L. G.; Buchholz, D.; Wu, L. M.; Vortmann, B.; Passerini, S. Unexpected performance of layered sodium-ion cathode material in ionic liquid-based electrolyte. *J. Power Sources* **2014**, *247*, 377−383.

(47) Park, K.; Han, D.; Kim, H.; Chang, W. S.; Choi, B.; Anass, B.; Lee, S. Characterization of a P2-type chelating-agent-assisted Na2/3Fe1/2Mn1/2O2 cathode material for sodium-ion batteries. *RSC Adv.* **2014**, *4* (43), 22798−22802.

(48) Bhaskar, A.; Krueger, S.; Siozios, V.; Li, J.; Nowak, S.; Winter, M. Synthesis and Characterization of High-Energy, High-Power Spinel-Layered Composite Cathode Materials for Lithium-Ion Batteries. *Adv. Energy Mater.* **2015**, *5* (5), 1401156.

(49) Yi, L. H.; Liu, Z. S.; Yu, R. Z.; Zhao, C. X.; Peng, H. F.; Liu, M. H.; Wu, B.; Chen, M. F.; Wang, X. Y. Li-Rich Layered/Spinel Heterostructured Special Morphology Cathode Material with High Rate Capability for Li-Ion Batteries. *ACS Sustainable Chem. Eng.* **2017**, *5* (11), 11005−11015.

(50) Luo, D.; Li, G. S.; Fu, C. C.; Zheng, J.; Fan, J. M.; Li, Q.; Li, L. P. A New Spinel-Layered Li-Rich Microsphere as a High-Rate Cathode Material for Li-Ion Batteries. *Adv. Energy Mater.* **2014**, *4* (11), 1400062.

(51) Nayak, P. K.; Grinblat, J.; Levi, M. D.; Haik, O.; Levi, E.; Talianker, M.; Markovsky, B.; Sun, Y. K.; Aurbach, D. Electrochemical Performance of a Layered-Spinel Integrated Li[Ni1/3Mn2/3]O-2 as a High Capacity Cathode Material for Li-Ion Batteries. *Chem. Mater.* **2015**, *27* (7), 2600−2611.

(52) Nayak, P. K.; Levi, E.; Grinblat, J.; Levi, M.; Markovsky, B.; Munichandraiah, N.; Sun, Y. K.; Aurbach, D. High-Capacity Layered-Spinel Cathodes for Li-Ion Batteries. *ChemSusChem* **2016**, *9* (17), 2404−2413.

(53) Wang, P. F.; Yao, H. R.; Liu, X. Y.; Zhang, J. N.; Gu, L.; Yu, X. Q.; Yin, Y. X.; Guo, Y. G. Ti-Substituted NaNi0.5Mn0.5-xTixO2 Cathodes with Reversible O3-P3 Phase Transition for High-Performance Sodium-Ion Batteries. *Adv. Mater.* **2017**, *29* (19), 1700210.

(54) McBreen, J. The application of synchrotron techniques to the study of lithium-ion batteries. *J. Solid State Electrochem.* **2009**, *13* (7), 1051−1061.

(55) Yoon, W. S.; Balasubramanian, M.; Chung, K. Y.; Yang, X. Q.; McBreen, J.; Grey, C. P.; Fischer, D. A. Investigation of the charge compensation mechanism on the electrochemically Li-ion deintercalated Li1-xCo1/3Ni1/3Mn1/3O2 electrode system by combination of soft and hard x-ray absorption spectroscopy. *J. Am. Chem. Soc.* **2005**, *127* (49), 17479−17487.

(56) Qiao, R. M.; Dai, K. H.; Mao, J.; Weng, T. C.; Sokaras, D.; Nordlund, D.; Song, X. Y.; Battaglia, V. S.; Hussain, Z.; Liu, G.; Yang, W. L. Revealing and suppressing surface Mn(II) formation of Na0.44MnO2 electrodes for Na-ion batteries. *Nano Energy* **2015**, *16*, 186−195.

(57) Ito, A.; Sato, Y.; Sanada, T.; Hatano, M.; Horie, H.; Ohsawa, Y. In situ X-ray absorption spectroscopic study of Li-rich layered cathode material Li[Ni0.17Li0.2Co0.07Mn0.56]O-2. *J. Power Sources* **2011**, *196* (16), 6828−6834.

(58) Oh, S. M.; Myung, S. T.; Yoon, C. S.; Lu, J.; Hassoun, J.; Scrosati, B.; Amine, K.; Sun, Y. K. Advanced Na-[Ni0.25Fe0.5Mn0.25]O-2/C-Fe$_3$O$_4$ Sodium-Ion Batteries Using EMS Electrolyte for Energy Storage. *Nano Lett.* **2014**, *14* (3), 1620−1626.

(59) Yue, J. L.; Yin, W. W.; Cao, M. H.; Zulipiya, S.; Zhou, Y. N.; Fu, Z. W. A quinary layer transition metal oxide of NaNi1/4Co1/4Fe1/4Mn1/8Ti1/8O2 as a high-rate-capability and long-cycle-life cathode material for rechargeable sodium ion batteries. *Chem. Commun.* **2015**, *51* (86), 15712−15715.

(60) Zhang, W.; Duchesne, P. N.; Gong, Z. L.; Wu, S. Q.; Ma, L.; Jiang, Z.; Zhang, S.; Zhang, P.; Mi, J. X.; Yang, Y. In Situ Electrochemical XAFS Studies on an Iron Fluoride High-Capacity Cathode Material for Rechargeable Lithium Batteries. *J. Phys. Chem. C* **2013**, *117* (22), 11498−11505.

(61) Ammundsen, B.; Jones, D. J.; Roziere, J.; Burns, G. R. Effect of chemical extraction of lithium on the local structure of spinel lithium manganese oxides determined by X-ray absorption spectroscopy. *Chem. Mater.* **1996**, *8* (12), 2799−2808.

(62) Lin, F.; Liu, Y. J.; Yu, X. Q.; Cheng, L.; Singer, A.; Shpyrko, O. G.; Xin, H. L. L.; Tamura, N.; Tian, C. X.; Weng, T. C.; Yang, X. Q.; Meng, Y. S.; Nordlund, D.; Yang, W. L.; Doeff, M. M. Synchrotron X-ray Analytical Techniques for Studying Materials Electrochemistry in Rechargeable Batteries. *Chem. Rev.* **2017**, *117* (21), 13123−13186.

(63) Yang, W.; Devereaux, T. P. Anionic and cationic redox and interfaces in batteries: Advances from soft X-ray absorption spectroscopy to resonant inelastic scattering. *J. Power Sources* **2018**, *389*, 188−197.

(64) Lin, F.; Nordlund, D.; Markus, I. M.; Weng, T. C.; Xin, H. L.; Doeff, M. M. Profiling the nanoscale gradient in stoichiometric layered cathode particles for lithium-ion batteries. *Energy Environ. Sci.* **2014**, *7* (9), 3077−3085.

(65) Liu, X. S.; Wang, D. D.; Liu, G.; Srinivasan, V.; Liu, Z.; Hussain, Z.; Yang, W. L. Distinct charge dynamics in battery electrodes revealed by in situ and operando soft X-ray spectroscopy. *Nat. Commun.* **2013**, *4*, 2568.

(66) Qiao, R. M.; Wang, Y. S.; Olalde-Velasco, P.; Li, H.; Hu, Y. S.; Yang, W. L. Direct evidence of gradient Mn(II) evolution at charged states in LiNi0.5Mn1.5O4 electrodes with capacity fading. *J. Power Sources* **2015**, *273*, 1120−1126.

(67) Hunter, J. C. Preparation of a New Crystal Form of Manganese-Dioxide - Lambda-Mno2. *J. Solid State Chem.* **1981**, *39* (2), 142−147.

(68) Yang, S. L.; Wang, D. N.; Liang, G. X.; Yiu, Y. M.; Wang, J. J.; Liu, L. J.; Sun, X. L.; Sham, T. K. Soft X-ray XANES studies of various phases related to LiFePO4 based cathode materials. *Energy Environ. Sci.* **2012**, *5* (5), 7007−7016.

(69) Brown, I. D.; Shannon, R. D. Empirical Bond-Strength Bond-Length Curves for Oxides. *Acta Crystallogr., Sect. A: Cryst. Phys., Diffr., Theor. Gen. Crystallogr.* **1973**, *29* (May1), 266−282.